Astronomy & Astrophysics

JWST imaging of the closest globular clusters

III. Multiple populations along the low-mass main-sequence stars of NGC 6397

M. Scalco[1,2] , M. Libralato[2] , R. Gerasimov[3] , L. R. Bedin[2] , E. Vesperini[4], D. Nardiello[5,2], A. Bellini[6] ,
M. Griggio[1,2,6] , D. Apai[7,8] , M. Salaris[9], A. Burgasser[10], and J. Anderson[6]

[1] Dipartimento di Fisica e Scienze della Terra, Università di Ferrara, Via Giuseppe Saragat 1, Ferrara 44122, Italy
[2] Istituto Nazionale di Astrofisica, Osservatorio Astronomico di Padova, Vicolo dell'Osservatorio 5, Padova 35122, Italy
  e-mail: michele.scalco@inaf.it
[3] Department of Physics and Astronomy, University of Notre Dame, Nieuwland Science Hall, Notre Dame, IN 46556, USA
[4] Department of Astronomy, Indiana University, Swain West, 727 E. 3rd Street, Bloomington, IN 47405, USA
[5] Dipartimento di Fisica e Astronomia "Galileo Galilei", Università di Padova, Vicolo dell'Osservatorio 3, 35122 Padova, Italy
[6] Space Telescope Science Institute, 3700 San Martin Drive, Baltimore, MD 21218, USA
[7] Department of Astronomy and Steward Observatory, The University of Arizona, 933 N. Cherry Avenue, Tucson, AZ 85721, USA
[8] Lunar and Planetary Laboratory, The University of Arizona, 1629 E. University Blvd., Tucson, AZ 85721, USA
[9] Astrophysics Research Institute, Liverpool John Moores University, 146 Brownlow Hill, Liverpool L3 5RF, UK
[10] Department of Astronomy & Astrophysics, University of California, San Diego, La Jolla, CA 92093, USA

ABSTRACT

Thanks to its exceptional near-infrared photometry, JWST can effectively contribute to the discovery, characterisation, and understanding of multiple stellar populations in globular clusters, especially at low masses where the *Hubble* Space Telescope (HST) faces limitations. This paper continues the efforts of the JWST GO-1979 programme in exploring the faintest members of the globular cluster NGC 6397. In this work, we show that the combination of HST and JWST data allows us to identify two groups of MS stars: MSa, the first-generation group, and MSb, the second-generation group. We measured the ratio between the two groups and combined it with measurements from the literature focused on more central fields and more massive stars compared to our study. Our findings suggest that the MSa and MSb stars are present in a ≈30−70 ratio regardless of the distance from the centre of the cluster and the mass of the stars used so far. However, considering the limited areal coverage of our study, a more comprehensive spatial analysis is necessary to definitively confirm complete spatial mixing.

Key words. techniques: photometric – catalogs – Hertzsprung-Russell and C-M diagrams – stars: Population II – globular clusters: individual: NGC 6397

1. Introduction

Many important questions in the study of globular clusters (GCs) benefit from the exquisite near-infrared (NIR) astrometry and photometry JWST can provide. An example is the phenomenon of the multiple stellar populations (mPOPs; for a recent review, see Gratton et al. 2019). Multiple stellar populations in GCs have been extensively studied for decades using the *Hubble* Space Telescope (HST; since Bedin et al. 2004). The ultraviolet and optical photometry provided by HST are particularly effective in disentangling the mPOPs in colour-magnitude (CMD) and colour-colour diagrams (e.g. Milone et al. 2017), spanning from the red giant branch (RGB) to the main sequence (MS). However, as stars become fainter and redder, the effectiveness of UV filters diminishes. While optical filters maintain high photometric precision for observing MS stars, they alone may not always permit the identification of mPOPs, as they lack the necessary information to differentiate stars with varying levels of oxygen, carbon, and nitrogen enhancement.

For these reasons, the analysis of mPOPs along the low-mass portion of the MS has predominantly relied on NIR filters (see Scalco et al. 2024, and reference therein) despite the inferior quality of HST's NIR data compared to UV/optical detectors.

The new generation of detectors on board JWST now provide high-resolution deep NIR images, enabling continued exploration of mPOPs along the MS of GCs and potentially advancing it further, as indicated by preliminary studies (Nardiello et al. 2022; Milone et al. 2023; Ziliotto et al. 2023; Cadelano et al. 2023).

This paper is the third of a series aimed at investigating one of the closest GCs to the Sun: NGC 6397, which is a close-by (2.48 kpc; Baumgardt & Vasiliev 2021), metal-poor ([Fe/H] = −2.02; Harris 1996, 2010), and old (age = 12.6 Gyr; Correnti et al. 2018) GC. The first paper of the series, Bedin et al. (2024, hereafter Paper I) used data from the Near Infrared Camera (NIRCam, Rieke et al. 2023) on board JWST to characterise the white dwarf (WD) cooling sequence (CS) of this cluster, while the second paper, Gerasimov et al. (2024a, hereafter Paper II) is focused on the characterisation of the brown dwarfs (BDs) of NGC 6397.

The presence of mPOPs in this stellar system was initially explored by Milone et al. (2012a) using data obtained with HST. Milone et al. (2012a) found that the MS of the cluster splits into two distinct components. One component (namely MSa) consists of a primordial population that resembles the composition of field stars. The other component (MSb) corresponds to

a second generation of stars characterised by enhanced sodium and nitrogen levels, reduced carbon and oxygen content, and a slightly increased helium abundance. The authors also found that MSb stars are more numerous (~70% of the total) than MSa stars (~30%). In this work, we make use of the astro-photometric catalogue of Paper I to analyse the mPOPs in the lower MS of NGC 6397.

The paper is organised as follows. Section 2 provides a summary of the dataset and reduction. Section 3 describes the identification of the mPOPs, the isochrone fit, and the radial and mass distribution of the two populations. Conclusions are presented in Sect. 4.

2. Observations and data reduction

The data were obtained as part of three programmes:

- HST GO-10424 (PI: Richer; taken in ~2005.2). This set comprises images (with a combination of long and short exposure times) taken with the Wide Field Channel (WFC) of the Advanced Camera for Surveys (ACS) in $F606W$ and $F814W$ filters.
- HST GO-11633 (PI: Rich; taken in ~2010.2). As before, this dataset includes both long and short exposures in ACS/WFC $F606W$ and $F814W$ filters.
- JWST GO-1979 (PI: Bedin; taken in ~2023.2). The JWST data were obtained with the NIRCam in $F150W2$ and $F322W2$ filters.

Figure 1 shows the position of our datasets in the field of view (FOV) overlaid on a Digital Sky Survey[1] (DSS) image of NGC 6397.

We made use of calibrated but un-resampled exposures (_flc and _cal fits files for HST and JWST, respectively). The data reduction was performed as described in Paper I, that is, a combination of first- and second-pass photometry for HST (see Bellini et al. 2017a, 2018; Nardiello et al. 2018; Libralato et al. 2018, 2022; Scalco et al. 2021, for details) and JWST images (see Nardiello et al. 2022, 2023; Griggio et al. 2023; Libralato et al. 2023, 2024, for details). The astrometry was anchored to an absolute reference-frame system provided by the *Gaia* Data Release 3 (DR3) catalogue (Gaia Collaboration 2016, 2023), and the photometry was calibrated to the VEGA-magnitude photometric system. Proper motions (PMs) were calculated by measuring the displacements between the JWST observations and the earliest HST observations, covering a temporal baseline of ~18 years. Detailed descriptions of the datasets and reduction are provided in Paper I.

The complete catalogue contains spurious detections such as cosmic rays or noise peaks in individual images. For this work, only a subset of well-measured cluster members was selected using the procedure outlined in Appendix A of Paper I. This selection process was based on diagnostic parameters such as the quality-of-PSF fit parameter (QFIT), the excess or deficiency of the source's flux (RADXS, see Bedin et al. 2008), the local sky noise (rmsSKY), and the utilisation of PM-based memberships criteria.

3. The split of the main sequence in NGC 6397 at lower stellar masses

Milone et al. (2012a) focused on the upper part of the MS within the mass range of ~0.56 to ~0.62 $M_\odot$ covering the central region
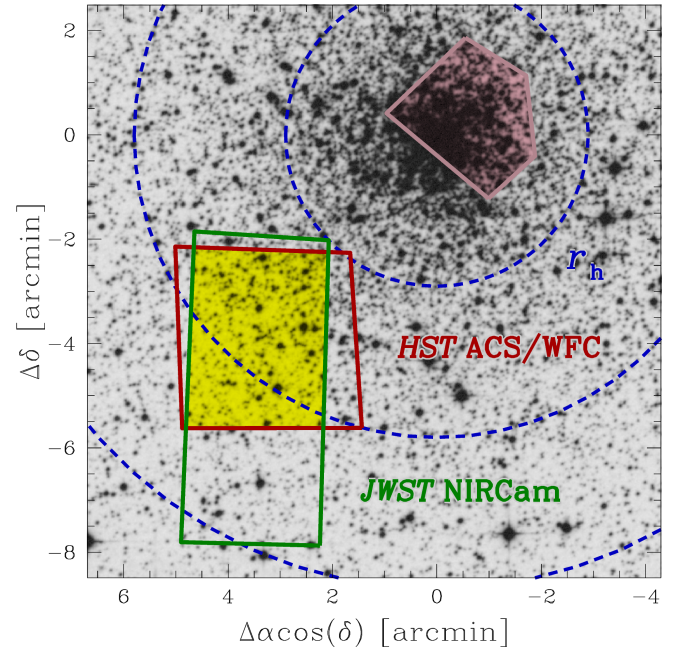

Fig. 1. Outlines of the ACS/WFC HST field observed under the GO-10424 and GO-11633 programmes (in red) and the NIRCam JWST field observed under the GO-1979 programme (in green) superimposed on a DSS image of NGC 6397. The region where the two datasets overlap is highlighted in yellow. We also show (in magenta) the field analysed in Milone et al. (2012a). The units are in arcminutes measured from the centre of the cluster. The blue dashed circles mark the half-light radius (r_h = 2.90; Harris 1996, 2010), $2\,r_h$ and $3\,r_h$.

of the cluster spanning from the centre to ~2 arcmin (equivalent to ~0.7 r_h). In this study, we used our HST and JWST datasets to investigate the two populations in the lower part of the MS, with masses ranging from ~0.09 to ~0.18 $M_\odot$ in an outer region spanning from ~3.2 to ~7 arcmin (equivalent to ~1.1 r_h to ~2.4 r_h) of NGC 6397.

We followed the methodology outlined by Milone et al. (2012b, see also Sarajedini et al. 2007; Bellini et al. 2017b) to correct our photometry for differential reddening and photometric zero-point variations across the FOV. Then, we made use of two-pseudo-colour diagrams (TpCDs, see Milone et al. 2015a,b) to identify the two groups of stars in the MS of NGC 6397.

Panels a and c of Fig. 2 respectively present the differential-reddening and zero-point corrected m_{F150W2} versus $m_{F814W} - m_{F322W2}$ and m_{F150W2} versus $m_{F606W} - m_{F150W2}$ CMDs. In each CMD, we have drawn by hand two fiducial curves enclosing the MS (represented in green in panels a and c) that were used to rectify the sequence. The rectified CMDs are presented in panels b and d, where $\Delta_{F814W-F322W2}$ and $\Delta_{F606W-F150W2}$ denote the $m_{F814W} - m_{F322W2}$ and $m_{F606W} - m_{F150W2}$ rectified and normalised pseudo-colours, respectively. Two sequences are faintly discernible in these diagrams; one is more populated on the red side of the plot, and the other is less populated on the blue side of the plot.

We combined the two verticalised diagrams to construct the TpCD (panel e). Panel f displays the Hess diagram of the TpCD, colour-coded according to the local density of points. The colour goes from blue (lowest density) to green (average density) to red (highest density). Two components are visible: a clump around (0.65, 0.60) representing the bump of MSb stars and a
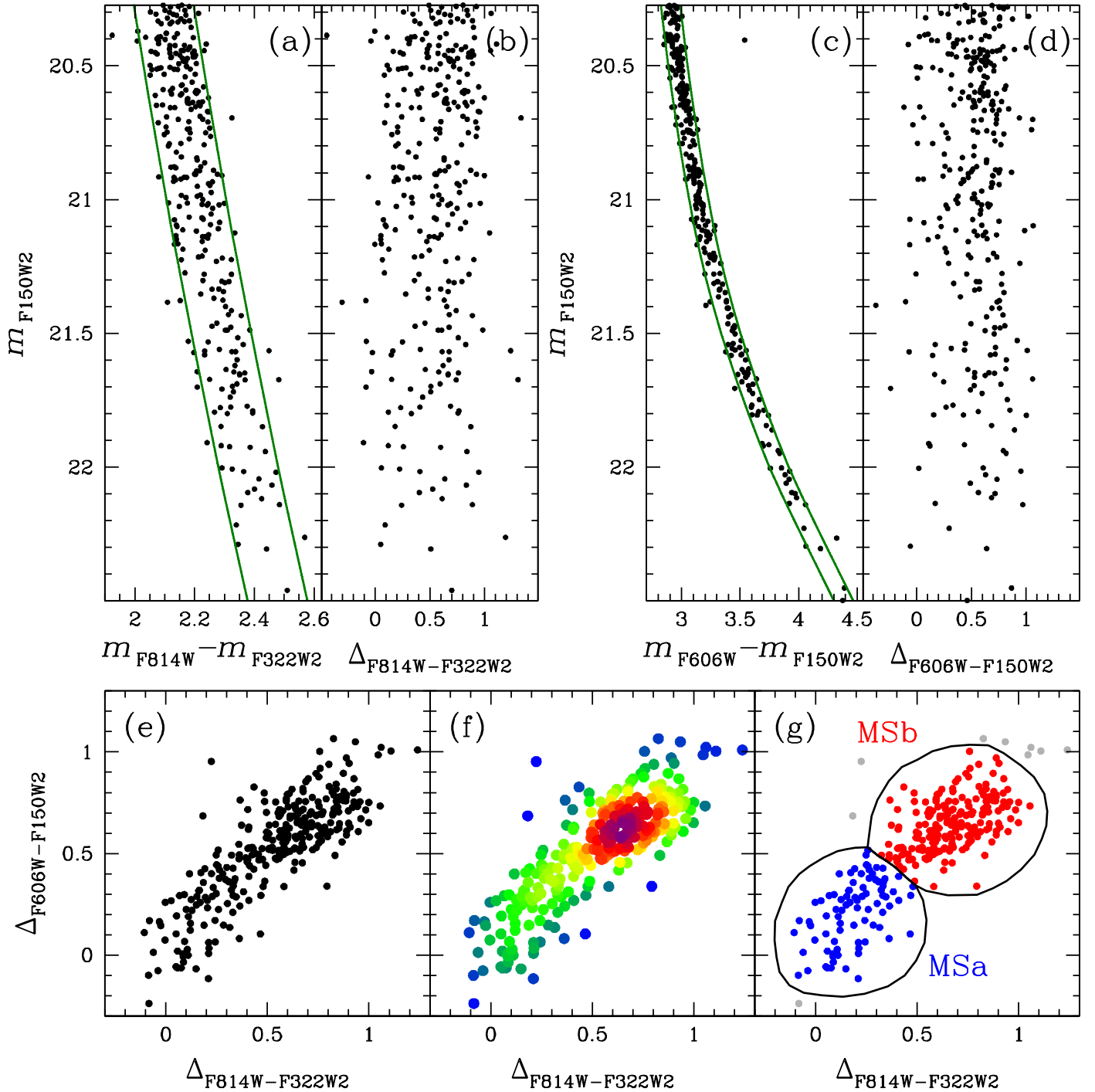
Fig. 2. Procedure used to identify the two sequences of stars in the lower part of the MS of NGC 6397. Panel a: m_{F150W2} versus $m_{F814W} - m_{F322W2}$ CMD of the stars in our sample, corrected for differential reddening and photometric zero-point variations. The two green lines (drawn by hand) are used to rectify the diagram. Panel b: rectified m_{F150W2} versus $\Delta_{F814W-F322W2}$ CMD. Panels c and d: same as a and b but for the m_{F150W2} versus $m_{F606W} - m_{F150W2}$ CMD. Panel e: $\Delta_{F606W-F150W2}$ versus $\Delta_{F814W-F322W2}$ TpCD. Panel f: Hess diagram of the TpCD. Panel g: two stellar populations identified in the TpCD (within the black envelopes), MSa (in blue) and MSb (in red). Stars outside the black envelopes are represented in grey.

tail extending towards the lower-left part of the plot representing the MSa stars.

The black envelopes (hand-defined) in panel g tentatively delineate the two components in the TpCD, with MSa stars in blue and MSb stars in red. Stars outside the envelopes were rejected and are represented in grey. We note that this figure represents an initial exploration, and a more detailed quantitative analysis will follow. The MSa component comprises 84 stars,

representing 29% ± 4% of the total, while the MSb component comprises 201 stars, representing 71% ± 6% of the total. The errors in this and the subsequent fractions are estimated by linear propagation of Poisson noise. These values are consistent with those reported in Milone et al. (2012a, ~30% ± 3% for the MSa and ~70% ± 3% for the MSb).

To better estimate the number of stars in each group while considering potential contamination between the populations,
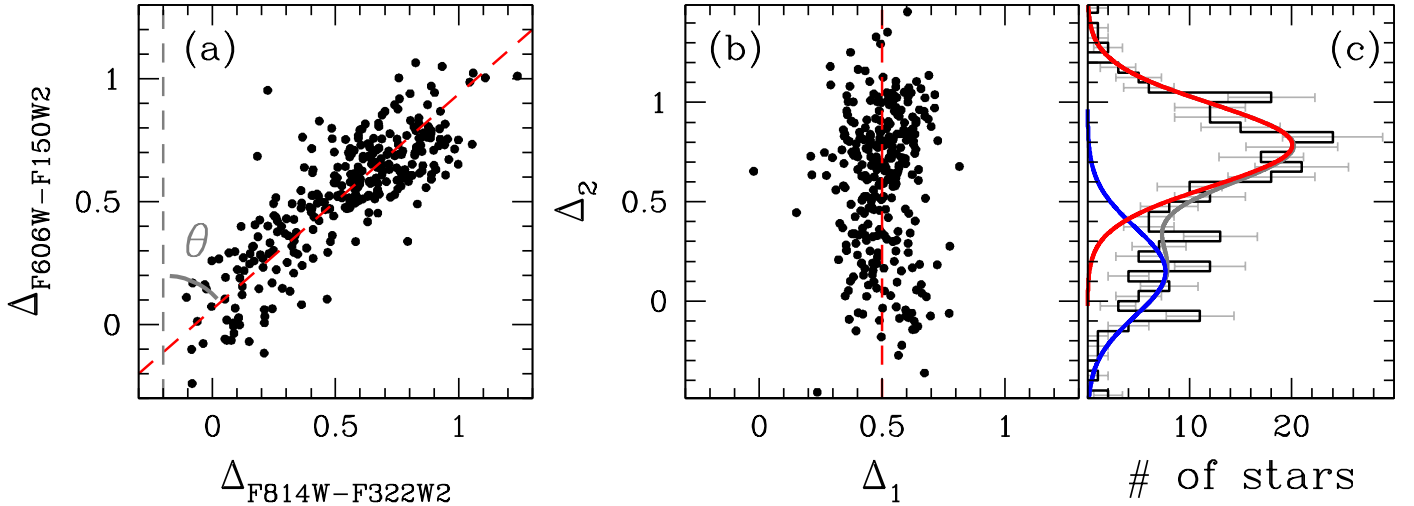
Fig. 3. Procedure to estimate the fraction of stars in the two populations. Panel a: same TpCD presented in panel e of Fig. 2. The red dashed line defines an angle θ with the y-axis. Panel b: Δ_2 versus Δ_1 diagram obtained by the counterclockwise rotation of panel a by an angle θ around the point $(0.5, 0.5)$. Panel c: histogram of the Δ_2 distribution with error bars representing Poisson errors. The best-fitting double-Gaussian function is represented in grey, while the two components are plotted in blue and red.

we adopted an alternative approach. Panel a of Fig. 3 displays the same TpCD as presented in panel e of Fig. 2. Initially, we fitted a straight line to the barycentres of the two populations in the TpCD (red dashed line), defining an angle θ with respect to the y-axis of the plot. Panel b shows the Δ_2 versus Δ_1 diagram obtained by a counterclockwise rotation of the TpCD by an angle θ around the point $(0.5, 0.5)$ so as to have the red line parallel to the y-axis. Finally, panel c presents the histogram of the Δ_2 distribution, with error bars representing Poisson errors. We fitted a double-Gaussian function to the histogram (depicted in grey) with the two components associated with MSa and MSb represented in blue and red, respectively. Once again, we determined that MSa and MSb respectively comprise $29\% \pm 4\%$ and $71\% \pm 6\%$ of the total. These values are in agreement with those obtained previously.

We assessed the robustness of our fitting method using a Gaussian mixture model (GMM) on the Δ_2 star distribution, employing the expectation-maximisation algorithm from the `scikit-learn` package (Pedregosa et al. 2011). To determine the optimal number of Gaussian components for the Δ_2 distribution, we calculated the Bayesian information criterion (BIC) for models with one to five Gaussian components. The first panel of Fig. 4 shows the BIC as a function of the number of Gaussian components, with the two-Gaussian model having the lowest BIC. The second panel of Fig. 4 presents the histogram of the Δ_2 distribution fitted with the two-Gaussian model. To further ensure robustness, we repeated the GMM fitting process 1000 times. In each iteration, we randomly selected 300 stars from our sample and calculated the fraction of stars in each MS. The third and fourth panels of Fig. 4 display the distribution of the ratio of the two populations from these 1000 iterations. The reported values are the median and standard deviation of the distribution, which are consistent with the values obtained from the analysis discussed earlier.

3.1. Isochrone fit

At the range of effective temperatures considered in this study (lower MS below the MS knee, $T_{\rm eff} = 3000-4000$), broadband photometry is primarily influenced by the abundances of

oxygen and titanium due to their role in molecular opacity (Gerasimov et al. 2024b). Since the member-to-member scatter in [O/Fe] is the primary tracer of mPOPs in GCs, the individual populations can be identified in the CMD through a careful selection of photometric bands. The $F322W2$ band of NIRCam is particularly sensitive to the oxygen abundance due to its proximity to the fundamental vibrational bands of water near 3 (Jørgensen et al. 2001). The second band is most well placed in the optical regime, where H_2O absorption is minimal; however, wavelengths redder than ~ 0.7 are preferred to avoid the strongest electronic bands of TiO (Plez 1998). Of the filters considered in this work, the $F814W$ band of ACS is the most suitable. The oxygen content of individual stars in NGC 6397 can be inferred from the $m_{F814W} - m_{F322W2}$ colour with minimal systematic errors due to potentially unknown abundances of other elements.

To derive [O/Fe] from photometry, we first chose a model isochrone from the `SANDee` grid (Paper II; Alvarado et al., in prep.) that provides the best representation of the m_{F150W2} versus $m_{F814W} - m_{F322W2}$ and m_{F150W2} versus $m_{F606W} - m_{F150W2}$ CMDs. The chosen isochrone had [Fe/H] $= -1.75$ and [α/Fe] $= 0.3$. We then calculated five new model isochrones varying [O/Fe] from -0.1 to 0.7 in steps of 0.2. The oxygen abundance was updated in the model atmospheres of the best-fit `SANDee` isochrone with $\log(g) \geq 4$ as were the corresponding evolutionary models and boundary condition tables, following Gerasimov et al. (2024b, 2022). For all new isochrones, we adopted the age of 12.6 Gyr from Correnti et al. (2018), the distance of 2.458 kpc from Baumgardt & Vasiliev (2021), and the optical reddening of $E(B - V) = 0.18$ from Gratton et al. (2003). The isochrones are overplotted on the observed CMD in the upper panel of Fig. 5.

The model isochrones for other oxygen abundances were obtained by linearly interpolating or extrapolating the mass-colour and mass-magnitude relationships. The values of [O/Fe] for individual stars were then determined by searching for the interpolated isochrones that pass through the observed colours and magnitudes using Brent's method (Brent 1973). Overall, the oxygen abundance of ~ 300 members of NGC 6397 was measured. The distribution of these measurements is shown in the lower panel of Fig. 5. The modal values of [O/Fe] for the two populations in the cluster were taken as the central values of
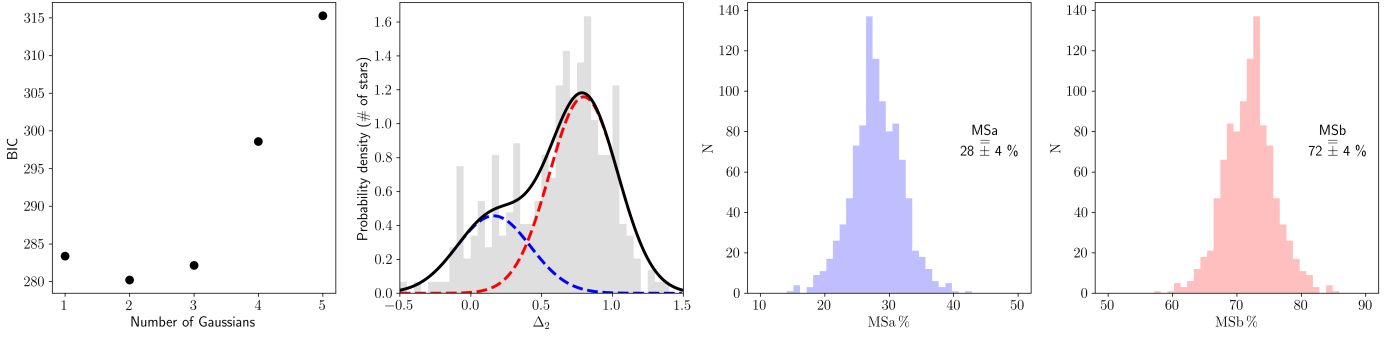
Fig. 4. Analysis of the Δ_2 distribution using GMM. First panel: BIC as a function of the number of Gaussian components considered in the GMM. Second panel: histogram of the Δ_2 distribution fitted with a two-Gaussian model (black continuous line). The two components of the two-Gaussian model are plotted as blue and red dashed lines. Third and fourth panels: distribution of the ratio of the two populations obtained from 1000 repetitions of the GMM fitting process. The reported values represent the median and standard deviation of the distribution.

Table 1. Effect of choosing a different base model isochrone on the oxygen abundances of individual stars.

Change in base isochrone	Expected offset in [O/Fe]
Increase [α/Fe] by 0.2	+0.18
Decrease [Fe/H] by 0.2	−0.12
Increase $E(B-V)$ by 0.02	+0.09
Decrease age by 2 Gyr	−0.002

the Gaussian components in a two-component Gaussian mixture fit to the inferred distribution. The fit was carried out using the expectation-maximisation algorithm implemented in the `scikit-learn` package. The two-component fit is shown in the lower panel of Fig. 5. The modal values of [O/Fe] were estimated as 0.32 ± 0.02 and 0.61 ± 0.02 for the two populations. We also estimated the expected systematic offsets in our [O/Fe] measurements by comparing other possible choices for the best-fit `SANDee` isochrone to the isochrones used in this work. The results of this analysis are summarised in Table 1.

In Milone et al. (2012a), the representative [O/Fe] of the two populations were estimated as 0.1 and 0.45 based on the differences between observed colours and model atmospheres. The values found in this work are ~0.2 higher. This discrepancy can be reconciled only by reducing the metallicity of the best-fit isochrone by ~0.3−0.4, that is, by setting it to [Fe/H] ~ −2. The implied lower metallicity would in fact be more consistent with other photometric (Correnti et al. 2018) and spectroscopic (Husser et al. 2016) estimates in the literature. The higher metallicity of NGC 6397 computed in this work near the end of the MS is likely due to imperfectly modelled physical processes in low-temperature stellar atmospheres, such as the depletion of gas-phase elements onto dust grains or non-equilibrium chemistry. A similar effect has been observed in a different NIRCam field of the cluster (Paper II). The relative difference in [O/Fe] between the two populations is approximately equal to that determined by Milone et al. (2012a), confirming the correspondence between the cluster populations identified in both studies.

3.2. Radial and mass distribution of the two populations

Although the fractions of the two populations obtained in our study generally align with those reported by Milone et al. (2012a), we subdivided our sample in order to investigate poten-

tial dependencies of these populations on the radial distance from the cluster's centre and stellar mass. To do this, we considered the two groups of stars defined in panel g of Fig. 2.

Panel a of Fig. 6 illustrates the spatial distribution of the two stellar populations in the $X-Y$ plane. Points are colour-coded as in panel g of Fig. 2. The two populations show no clear difference in their spatial distributions.

We examined the radial profile of the relative number of the two populations by dividing the stars into two equally populated radial bins. We then evaluated for each bin the ratio of the MSa population relative to the total number of stars in that bin. Panel b of Fig. 6 shows our measurements (filled circles) together with the values reported by Milone et al. (2012a, triangles) and Milone et al. (2017, squares) for the central part of the cluster. It is important to note that each dataset corresponds to different mass ranges (see discussion below). The combined dataset spans a radial distance from the centre of the cluster out to ~7 arcmin, corresponding to ~2.4 $r_{\rm h}$. This comprehensive analysis demonstrates that the two populations of NGC 6397 have reached complete spatial mixing. NGC 6397 has a half-mass relaxation time of $t_{\rm rh} \sim 0.5$ Gyr (Vasiliev & Baumgardt 2021) and is thus a dynamically old cluster (age/$t_{\rm rh} \sim 25$; see also Giersz & Heggie 2009). Various investigations studying the dynamical evolution of multiple-population clusters (see e.g. Vesperini et al. 2013, 2021; Dalessandro et al. 2019) have predicted that in clusters with this dynamical age, the two populations should indeed be completely mixed and have lost memory of any initial spatial differences.

Finally, panel c of Fig. 6 presents the population ratio as a function of stellar mass. The average mass of the stars was inferred by means of the isochrones presented in Fig. 5. We divided our sample into two equally populated mass bins and evaluated the ratio of the MSa population in each bin. Our estimates are represented in panel c along with the values reported by Milone et al. (2012a, 2017) using the same symbols as in panel b. Similarly to what was found in the analysis of the radial distribution of the two populations, we find that the fraction of stars in the two populations is also independent of the stellar mass. This result is consistent, in general, with what was found for other clusters (e.g. Milone et al. 2019, 2023; Dondoglio et al. 2022; Ziliotto et al. 2023). We note that since different mass intervals are studied in different radial regions in our analysis, we could not carry out a consistent analysis of the stellar mass function of the two populations and its radial variation (see e.g. King et al. 1995, for a study of mass segregation and radial variation of the stellar mass function in this cluster).
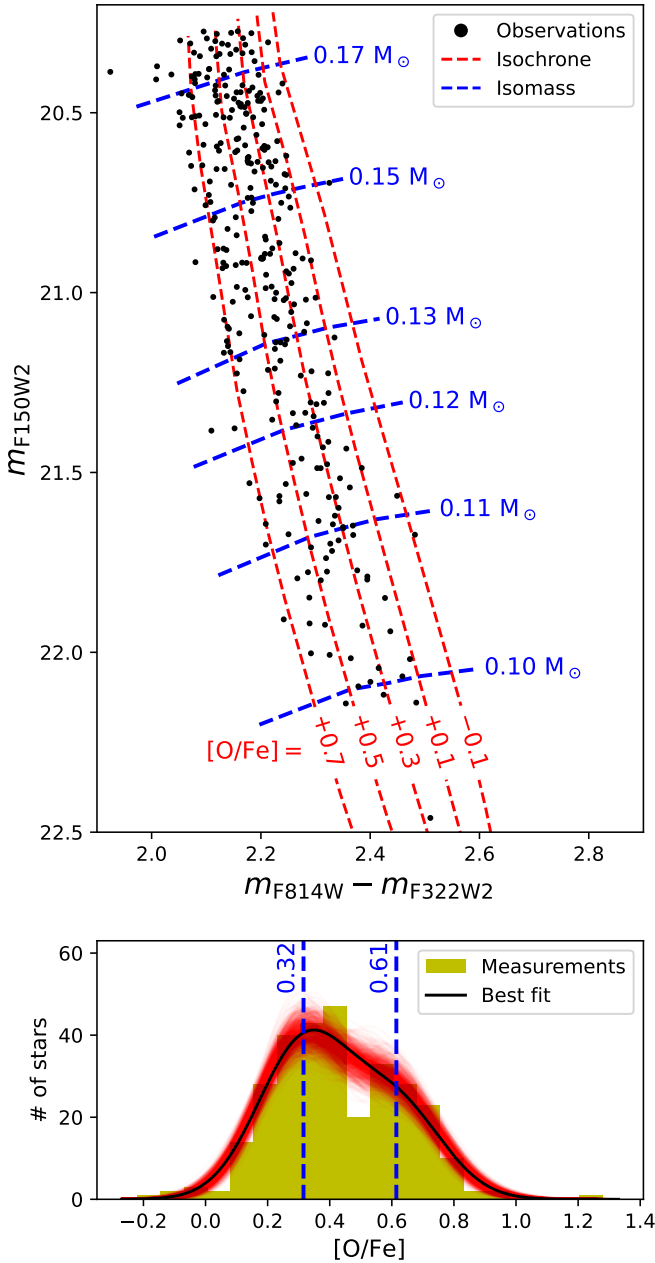
Fig. 6. Analysis of the radial an mass distribution of the two populations. Panel a: spatial distribution of the two populations in the $X-Y$ plane. Points are colour-coded as in panel g of Fig. 2. Panel b: fraction of MSa stars as a function of radial distance from the centre of the cluster, R. The values obtained in this work are represented with circles, while the estimates from Milone et al. (2012a, 2017) are shown with triangles and squares, respectively. Each dataset corresponds to different mass ranges (see panel c). The grey dashed lines are set at r_h and $2\,r_h$. Panel c: fraction of MSa stars as a function of stellar mass. Symbols have the same meaning as in panel b.

The components MSa and MSb are present in a $\approx 30-70$ ratio, which is consistent with findings from previous studies of NGC 6397 focused on its centremost region. By combining the results in this work with those from the literature, we found that the MSa/MSb ratio does not vary with the distance from the centre of the cluster. NGC 6397 is a dynamically old cluster, and this finding is consistent with the results of numerical studies predicting that the initial differences between the spatial distributions of mPOPs are gradually erased during the cluster's long-term evolution and are expected to be completely lost in the dynamically older clusters. However, due to the limited areal coverage of our study, this result should be interpreted with caution. A more extensive spatial coverage would be necessary to definitively confirm complete spatial mixing.

The JWST NIR photometry data analysed in this paper allowed us to probe and identify mPOPs in a low-mass interval ($\sim 0.09-0.18\,M_\odot$) that had never been studied before for this cluster. A comparison of our data with those of studies covering stellar mass intervals showed that the mass fraction is also independent of the stellar mass. This is consistent with what was found for other clusters (e.g. Milone et al. 2019, 2023; Dondoglio et al. 2022; Ziliotto et al. 2023) and could be used to put additional constraints on mPOP formation scenarios (see discussion in, e.g. Milone et al. 2023). We note that each of the three radial intervals analysed for this cluster covers different mass intervals, and the population ratio for different mass intervals was thus calculated at different radial distances. While we cannot a priori exclude the possibility that there are radial and mass dependencies cancelling each other and resulting in a population ratio independent of mass and radius, this would nonetheless be an unlikely coincidence. For a comprehensive investigation of the stellar mass function and its radial variation, future observations providing data covering the same mass range at different radial distances will be necessary.

Fig. 5. Isochrone fit and chemical study of the two populations. Top: model isochrones calculated in this study overplotted on NIRCam photometry of NGC 6397. The isochrones are labelled by the adopted oxygen abundance. Linearly interpolated isomass lines are shown for selected masses. Bottom: histogram of measured [O/Fe] values for the individual stars in the cluster. The best-fit two-component Gaussian mixture is overplotted, with the central values of both components indicated with vertical lines. The uncertainty in the best-fit distribution was estimated using 1000 bootstrap trials, shown with semi-transparent red lines.

4. Conclusions

This paper represents the third instalment in a series, and its focus is on the characterisation of the mPOPs in NIR within the lower MS of NGC 6397 using high-precision photometry with HST and JWST. The TpCD highlights the presence of two components, namely MSa and MSb, associated with a primordial and second-generation population, respectively.
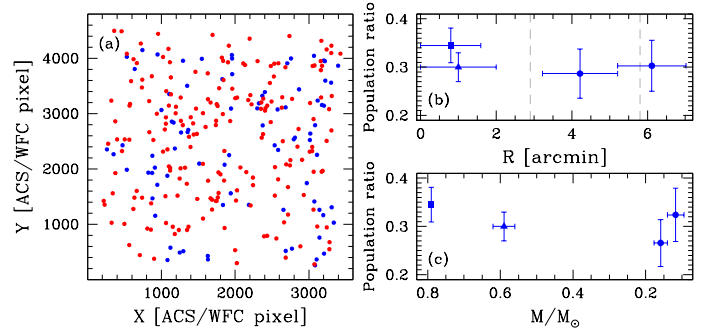
References

Baumgardt, H., & Vasiliev, E. 2021, MNRAS, 505, 5957
Bedin, L. R., Piotto, G., Anderson, J., et al. 2004, ApJ, 605, L125
Bedin, L. R., King, I. R., Anderson, J., et al. 2008, ApJ, 678, 1279
Bedin, L. R., Nardiello, D., Salaris, M., et al. 2024, Astron. Nachr., e20240039
Bellini, A., Anderson, J., Bedin, L. R., et al. 2017a, ApJ, 842, 6
Bellini, A., Anderson, J., van der Marel, R. P., et al. 2017b, ApJ, 842, 7
Bellini, A., Libralato, M., Bedin, L. R., et al. 2018, ApJ, 853, 86
Brent, R. P. 1973, SIAM J. Numer. Anal., 10, 327
Cadelano, M., Pallanca, C., Dalessandro, E., et al. 2023, A&A, 679, L13
Correnti, M., Gennaro, M., Kalirai, J. S., Cohen, R. E., & Brown, T. M. 2018, ApJ, 864, 147
Dalessandro, E., Cadelano, M., Vesperini, E., et al. 2019, ApJ, 884, L24
Dondoglio, E., Milone, A. P., Renzini, A., et al. 2022, ApJ, 927, 207
Gaia Collaboration (Prusti, T., et al.) 2016, A&A, 595, A1
Gaia Collaboration (Vallenari, A., et al.) 2023, A&A, 674, A1
Gerasimov, R., Burgasser, A. J., Homeier, D., et al. 2022, ApJ, 930, 24
Gerasimov, R., Bedin, L. R., Burgasser, A. J., et al. 2024a, ApJ, 971, 65
Gerasimov, R., Burgasser, A. J., Caiazzo, I., et al. 2024b, ApJ, 961, 139
Giersz, M., & Heggie, D. C. 2009, MNRAS, 395, 1173
Gratton, R. G., Bragaglia, A., Carretta, E., et al. 2003, A&A, 408, 529
Gratton, R., Bragaglia, A., Carretta, E., et al. 2019, A&ARv, 27, 8
Griggio, M., Nardiello, D., & Bedin, L. R. 2023, Astron. Nachr., 344
Harris, W. E. 1996, AJ, 112, 1487
Harris, W. E. 2010, ArXiv e-prints [arXiv:1012.3224]
Husser, T.-O., Kamann, S., Dreizler, S., et al. 2016, A&A, 588, A148
Jørgensen, U. G., Jensen, P., Sørensen, G. O., & Aringer, B. 2001, A&A, 372, 249
King, I. R., Sosin, C., & Cool, A. M. 1995, ApJ, 452, L33
Libralato, M., Bellini, A., Bedin, L. R., et al. 2018, ApJ, 854, 45
Libralato, M., Bellini, A., Vesperini, E., et al. 2022, ApJ, 934, 150
Libralato, M., Bellini, A., van der Marel, R. P., et al. 2023, ApJ, 950, 101
Libralato, M., Argyriou, I., Dicken, D., et al. 2024, PASP, 136, 034502
Milone, A. P., Marino, A. F., Piotto, G., et al. 2012a, ApJ, 745, 27
Milone, A. P., Piotto, G., Bedin, L. R., et al. 2012b, A&A, 540, A16
Milone, A. P., Marino, A. F., Piotto, G., et al. 2015a, MNRAS, 447, 927
Milone, A. P., Marino, A. F., Piotto, G., et al. 2015b, ApJ, 808, 51
Milone, A. P., Piotto, G., Renzini, A., et al. 2017, MNRAS, 464, 3636
Milone, A. P., Marino, A. F., Bedin, L. R., et al. 2019, MNRAS, 484, 4046
Milone, A. P., Marino, A. F., Dotter, A., et al. 2023, MNRAS, 522, 2429
Nardiello, D., Libralato, M., Piotto, G., et al. 2018, MNRAS, 481, 3382
Nardiello, D., Bedin, L. R., Burgasser, A., et al. 2022, MNRAS, 517, 484
Nardiello, D., Bedin, L. R., Griggio, M., et al. 2023, MNRAS, 525, 2585
Pedregosa, F., Varoquaux, G., Gramfort, A., et al. 2011, J. Mach. Learn. Res., 12, 2825
Plez, B. 1998, A&A, 337, 495
Rieke, M. J., Kelly, D. M., Misselt, K., et al. 2023, PASP, 135, 028001
Sarajedini, A., Bedin, L. R., Chaboyer, B., et al. 2007, AJ, 133, 1658
Scalco, M., Bellini, A., Bedin, L. R., et al. 2021, MNRAS, 505, 3549
Scalco, M., Gerasimov, R., Bedin, L. R., et al. 2024, Astron. Nachr., 345, e20240018
Vasiliev, E., & Baumgardt, H. 2021, MNRAS, 505, 5978
Vesperini, E., McMillan, S. L. W., D'Antona, F., & D'Ercole, A. 2013, MNRAS, 429, 1913
Vesperini, E., Hong, J., Giersz, M., & Hypki, A. 2021, MNRAS, 502, 4290
Ziliotto, T., Milone, A., Marino, A. F., et al. 2023, ApJ, 953, 62